Ensemble reconstruction of missing satellite data using a denoising diffusion model: application to chlorophyll a concentration in the Black Sea

Alexander Barth[1], Julien Brajard[2], Aida Alvera-Azcárate[1], Bayoumy Mohamed[1], Charles Troupin[1], and Jean-Marie Beckers[1]

[1]GHER, FOCUS, University of Liège, Liège, Belgium
[2]Nansen Environmental and Remote Sensing Center and Bjerknes Centre for Climate Research, Bergen N5007, Norway

Correspondence: A. Barth (a.barth@uliege.be)

Abstract. Satellite observations provide a global or near-global coverage of the World Ocean. They are however affected by clouds (among others), which severely reduce their spatial coverage. Different methods have been proposed in the literature to reconstruct missing data in satellite observations. For many applications of satellite observations, it has been increasingly important to accurately reflect the underlying uncertainty of the reconstructed observations. In this paper, we investigate the use of a denoising diffusion model to reconstruct missing observations. Such methods can naturally provide an ensemble of reconstructions where each member is spatially coherent with the scales of variability and with the available data. Rather than providing a single reconstruction, an ensemble of possible reconstructions can be computed, and the ensemble spread reflects the underlying uncertainty. We show how this method can be trained from a collection of satellite data without requiring a prior interpolation of missing data and without resorting to data from a numerical model. The reconstruction method is tested with chlorophyll a concentration from the Ocean and Land Color Instrument (OLCI) sensor (onboard the satellites Sentinel-3A and Sentinel-3B) on a small area of the Black Sea and compared with the neural network DINCAE (Data-Interpolating Convolutional Auto-Encoder). The spatial scales of the reconstructed data are assessed via a variogram, and the accuracy and statistical validity of the produced ensemble reconstructed are quantified using the continuous ranked probability score and its decomposition into reliability, resolution and uncertainty.

1 Introduction

At any given time, about 75 % of the ocean surface is covered by clouds (Wylie et al., 2005) which are opaque to electromagnetic radiation in the visible and infrared spectrum. Many satellite sensors rely on this part of the spectrum to measure, for example, sea surface temperature and ocean color. Besides clouds, other reasons for missing data include atmospheric dust, sun glint contamination, limited swath width, and high sensor-zenith angle (Feng and Hu, 2016; Mikelsons and Wang, 2019; Alvera-Azcàrate et al., 2021). The amount of missing data in satellite observations can therefore be substantial.

Several methods have been proposed in the past to reconstruct missing data in satellite images, such as EOF-based (Empirical Orthogonal Functions) methods like Data Interpolating Empirical Orthogonal Functions (DINEOF, Alvera-Azcárate et al., 2016; Alvera-Azcàrate et al., 2021; Pujol et al., 2022), optimal interpolation (*e.g.* Reynolds et al., 2007), and Kriging (*e.g.* Saulquin et al., 2011). More recently, neural network-based techniques, such as the Data-Interpolating Convolutional Auto-Encoder (DINCAE, Barth et al., 2020; Han et al., 2020; Ji et al., 2021; Jung et al., 2022; Barth et al., 2022; Luo et al., 2022) and other neural networks with a U-Net architecture (Ronneberger et al., 2015) like those described by Hong et al. (2023) as well as marked auto-encoders (Goh et al., 2023), have been applied to this problem. The input of these neural networks is typically a satellite image with missing data and the output is the reconstructed full field. Then the neural network is trained by being fed pairs of images (with and without clouds, or with some clouds and with even more clouds) so that the neural network learns the mapping between an image affected by clouds and a clear image.

While all geophysical measurements are potentially affected by errors, it is clear that for all reconstruction methods, the error of the reconstructed and initial missing pixels is typically expected to be larger than the error of the original pixels in a satellite image. In optimal interpolation and Kriging, this error is represented by the *a posteriori* error covariance. However, these methods assume that the errors can be described by a Gaussian distribution and that the underlying error covariances of the observations and the first guess are perfectly known. In practice, the error covariance of the first guess (the *a priori* error covariance) is often described as an isotropic function depending only on the distance between two points. In addition, these methods assume that the observations and the first guess are unbiased and independent.

For DINCAE, the estimation of the error variance is part of the training process and does not require precise knowledge of the error statistics of the input data. For every pixel, an estimate of the reconstructed value and its error variance is provided. During the training process, the likelihood of the actual measurement is maximized by assuming that the error is Gaussian distributed. This gives a pointwise estimate of the error variance and validation with independent data shows that the expected error variance is reliable. However, this approach does not give us any information about how the error is correlated in space (and time). This additional information is crucial for computing the expected error of derived quantities that combine satellite data from different spatial locations. For example, this is the case when computing an average quantity over a given area.

Another issue, when the model is forced to provide a single reconstruction, is that the results are often too smooth, as small scales under clouds are of course not resolved when the cloud coverage has a given spatial extension (and only large scales can be estimated using available data). Since multiple images would be coherent with the partial information present, a neural network trained to minimize e.g. the mean square error, would then implicitly produce the average of all these possible states. Consequently, this means that small scale information cannot be adequately retained.

Therefore, instead of creating a single reconstruction for each pixel (with the associated error variance), it would be preferable to produce an ensemble of likely reconstructions (based on the available data), as is the case with ensemble modeling and

the Ensemble Kalman Filter (Evensen, 2009). The expected error of a derived quantity (for example total amount of surface chlorophyll in a given area) is then given directly by the ensemble statistics where this derived quantity is computed for each member of the ensemble individually.

60   The denoising diffusion models (*e.g.* Ho et al., 2020) belong to the family of generative algorithms like Generative Adversarial Networks (Goodfellow et al., 2016). Contrarily to deterministic neural networks, in which the primary objective is to learn a mapping function between input features and a desired output, generative models aim to produce samples from the same distribution as the training data. In general, such probability distribution cannot be expressed explicitly in closed form. In many studies (*e.g.* Dhariwal and Nichol, 2021; Bayat, 2023), it has been shown empirically that diffusion models tend to have

65   better diversity than Generative Adversarial Networks which is an important property if one wants to represent the uncertainty of the reconstruction of incomplete satellite data.

Often diffusion models condition the reverse process by some information (for example text description or an image) in order to guide the generation process. This guidance can be implemented using a classifier to steer the generation process (Dhariwal and Nichol, 2021) which requires a pre-trained classifier suitable for noisy images.

70   In the classifier-free guidance algorithm (Ho and Salimans, 2022) the neural network denoising the images also depends explicitly on the class label. While training the neural network, this class label is sometimes replaced by a null label. During sampling the reverse diffusion is steered by a scaled difference between the noise predicted knowing the label and the noise predicted with a null label.

Denoising diffusion models have also been used for increasing the resolution (Saharia et al., 2021) and for in-painting.

75   Lugmayr et al. (2022) apply the forward and reverse diffusion process iteratively to fill in the missing region. However, for these approaches the diffusion model must be trained on a large collection of complete images.

In section 2, we will introduce the denoising diffusion framework which is the basis of this work. The data will be presented in section 3. The denoising diffusion framework will be adapted in section 4 to handle missing data during the training and to produce reconstructed images based on partial data. The results will be discussed and validated in the section 5 and compared

80   to the DINCAE method. Conclusions will be presented in section 6.

2   Denoising diffusion model

The denoising diffusion models (Ho et al., 2020) use a quite different approach than traditional applications for neural networks, as their goal is to generate an image that comes from the same (but not explicitly known) distribution as the training data. This inherently stochastic generation process gives us an appropriate framework to provide an ensemble of possible states.

85

The present description closely follows Ho et al. (2020). The general idea is that we start with a clear image $\mathbf{x}_0$ (later we will discuss the case where all training images contain clouds) and then progressively add noise. Without loss of generality, we assume that $\mathbf{x}_0$ is scaled such that every element is of the order of 1. In practice, we remove the mean and divide the anomalies

by the standard deviation. The mean and standard deviation are here single scalars computed over the whole training dataset.

90

The diffusion process is a Markov process as every image $\mathbf{x}_t$ (considered here as a flat vector) depends only on the previous image $\mathbf{x}_{t-1}$ in this chain. We degrade the image $\mathbf{x}_{t-1}$ by adding noise $\mathbf{z}_t$ ($\mathbf{z}_t \sim \mathcal{N}(0,\mathbf{I})$) scaled by the parameter β_t (with $0 < \beta_t < 1$). At the same time, we scale the image $\mathbf{x}_{t-1}$ so that the combination $\mathbf{x}_t$ remains of unit variance:

$$\mathbf{x}_t = \sqrt{1-\beta_t}\mathbf{x}_{t-1} + \sqrt{\beta_t}\mathbf{z}_{t-1} \tag{1}$$

95   This Markov process has the following transition probability (also called forward diffusion kernel):

$$q(\mathbf{x}_t|\mathbf{x}_{t-1}) = N(\mathbf{x}_t; \sqrt{1-\beta_t}\mathbf{x}_{t-1}, \beta_t\mathbf{I}) \tag{2}$$

The linear combination of two Gaussian distributed variables is also Gaussian distributed. Therefore, we can compute the transition probability $q(\mathbf{x}_t|\mathbf{x}_0)$ in closed form (Ho et al., 2020):

$$q(\mathbf{x}_t|\mathbf{x}_0) = N(\mathbf{x}_t; \sqrt{\bar{\alpha}_t}\mathbf{x}_0, \bar{\alpha}_t\mathbf{I}) \tag{3}$$

100   where $\bar{\alpha}_t = \prod_{s=1}^{t}\alpha_s$ and $\alpha_t = 1-\beta_t$. All elements α_t are smaller than 1, therefore, $\bar{\alpha}_t$ tends to zero as t increases. The image $\mathbf{x}_t$ will become more and more similar to an image with Gaussian noise as t increases. The last image $\mathbf{x}_T$ approximately follows a Gaussian distribution with zero mean and an identity matrix as covariance:

$$q(\mathbf{x}_T) \approx \mathcal{N}(\mathbf{x}_T; 0, \mathbf{I}) \tag{4}$$

2.1 Reverse process

105   If the forward transition kernel is a Gaussian distribution, the distribution of the reverse transition kernel is also a Gaussian distribution in the limit of small steps sizes β (Feller, 1949; Sohl-Dickstein et al., 2015). The Markov chain for the reverse process begins with a Gaussian Distribution random variable with zero mean and unit variance:

$$p(\mathbf{x}_T) = \mathcal{N}(\mathbf{x}_T; 0, \mathbf{I}) \tag{5}$$

The reverse process is also a Markov process involving the transition probabilities $p_{\boldsymbol{\theta}}(\mathbf{x}_{T-1}, \mathbf{x}_T)$ and a certain number of

110   model parameters $\boldsymbol{\theta}$ to be determined:

$$p_{\boldsymbol{\theta}}(\mathbf{x}_{T-1}) = \int p_{\boldsymbol{\theta}}(\mathbf{x}_{T-1}, \mathbf{x}_T)d\mathbf{x}_T \tag{6}$$

Formally, the probability of the clear image $\mathbf{x}_0$ is obtained by combining the probability of all possible trajectories $\mathbf{x}_{0:T}$ leading to the image $\mathbf{x}_0$:

$$p_{\boldsymbol{\theta}}(\mathbf{x}_0) = \int p_{\boldsymbol{\theta}}(\mathbf{x}_{0:T}) d\mathbf{x}_{1:T} \tag{7}$$

115 The parameters $\boldsymbol{\theta}$ will be determined by maximizing the probability $p_{\boldsymbol{\theta}}(\mathbf{x}_0)$, or equivalently by minimizing the negative logarithm of this probability:

$$L = -\log(p_{\boldsymbol{\theta}}(\mathbf{x}_0)) \tag{8}$$

In practice, the integral is intractable as it would require an integration over a very high-dimensional space. It can be shown that L is always smaller than the so-called evidence lower bound L_{elb} (Sohl-Dickstein et al., 2015) using Jensen's inequality 120 (Jensen, 1906) and the Bayes' theorem:

$$-\log(p_{\boldsymbol{\theta}}(\mathbf{x}_0)) \leq -E\left[\log \frac{p_{\boldsymbol{\theta}}(\mathbf{x}_{0:T})}{q(\mathbf{x}_{1:T})|\mathbf{x}_0}\right] = -E\left[\log\left(p_{\boldsymbol{\theta}}(\mathbf{x}_T) \prod_{t=1}^{T} \frac{p_{\boldsymbol{\theta}}(\mathbf{x}_{t-1}|\mathbf{x}_t)}{q(\mathbf{x}_t|\mathbf{x}_{t-1})}\right)\right] = L_{\text{elb}} \tag{9}$$

where the latent variables (i.e. unobserved variables) are here the whole trajectory except the first state ($\mathbf{x}_{1:T}$). Rather than minimizing L, the quantity L_{elb} is minimized instead. Ho et al. (2020) showed that this leads, after some simplifications, to the following cost function for training the neural network ($\epsilon_{\boldsymbol{\theta}}(\mathbf{x},t)$), for any step t and for any sample $\mathbf{x}_0$ from the training 125 dataset:

$$J(\boldsymbol{\theta}) = ||\boldsymbol{\epsilon} - \boldsymbol{\epsilon}_{\boldsymbol{\theta}}(\sqrt{\bar{\alpha}_t}\mathbf{x}_0 + \sqrt{1-\bar{\alpha}_t}\,\boldsymbol{\epsilon},t))||^2 \tag{10}$$

where $\boldsymbol{\epsilon}$ is the accumulated noise added during the forward process. The weights $\boldsymbol{\theta}$ of the neural network are updated using the gradient of the previous loss function. A trained neural network can then be used to create other samples $\mathbf{x}_0$ by solving the following equation backwards where the initial image $\mathbf{x}_T$ and $\mathbf{z}$ follows a normal distribution:

$$130 \quad \mathbf{x}_{t-1} = \frac{1}{\sqrt{\alpha_t}}\left(\mathbf{x}_t - \frac{1-\alpha_t}{\sqrt{1-\bar{\alpha}_t}}\boldsymbol{\epsilon}_{\boldsymbol{\theta}}(\mathbf{x}_t,t)\right) + \sigma_t\mathbf{z} \tag{11}$$

where the noise term σ_t is equal to $\sqrt{\beta_t}$. This algorithm will be extended in Section 4.1 to handle clouded images.

3 Data

To illustrate the application of the denoising diffusion model, we use the L3 satellite chlorophyll a concentration of the Black Sea at a spatial resolution of 300 m from the Copernicus Marine Service (Zibordi et al., 2015; Kajiyama et al., 2019; Lee

135 et al., 2002; European Union-Copernicus Marine Service, 2022) using data from the Ocean and Land Color Instrument (OLCI) sensor onboard the Sentinel-3A and Sentinel-3B satellites. On average, the amount of valid data over the ocean is 30% and shows a clear seasonal cycle (Figure 1). The marked increase of data after 2019 is due to the availability of Sentinel-3B data. We use data from April 26, 2016 to August 31, 2023 of this chlorophyll a concentration dataset. For the training data, we use data up to the date August 31, 2021. The training data is split horizontally in tiles with 64 x 64 grid cells. Only tiles with at

140 least 20% valid data (i.e. non-clouded pixels) are used for training. In total, there are 851926 images for training.

The validation and test data range from September 1, 2021 to August 31, 2022 and from September 1, 2022 to August 31, 2023, respectively. We only consider the region 28.56979°E - 28.80623°E and 43.64238°N - 43.81242°N (corresponding to a 64×64 grid at 300 m resolution) for validating and testing of the neural network (while the data from the whole Black Sea

145 is used for training), as the other considered method (DINCAE) has only been tested so far with a fixed location. This is a relatively small area, but it allowed us to perform several tests with different network configurations (Figure 2). The aim of the study is to test different methods on a problem with a similar size than the MNIST (Modified National Institute of Standards and Technology database) datasets (Yadav and Bottou, 2019) which is composed of 28×28 gray scale images of handwritten digits.

150 A coastal area was chosen because the dynamics there are more complex than in offshore waters. For the validation and test data, we randomly took the cloud mask from other time instances to mask additional grid cells which will be used for validation. Only images with a cloud mask between 15% and 35% of the missing data were considered as an additional mask to obtain a sufficient number of "clouded" pixels without masking an image almost entirely.

All the data is log transformed (base 10) and the units are to be understood as $\log_{10} \text{mg m}^{-3}$.
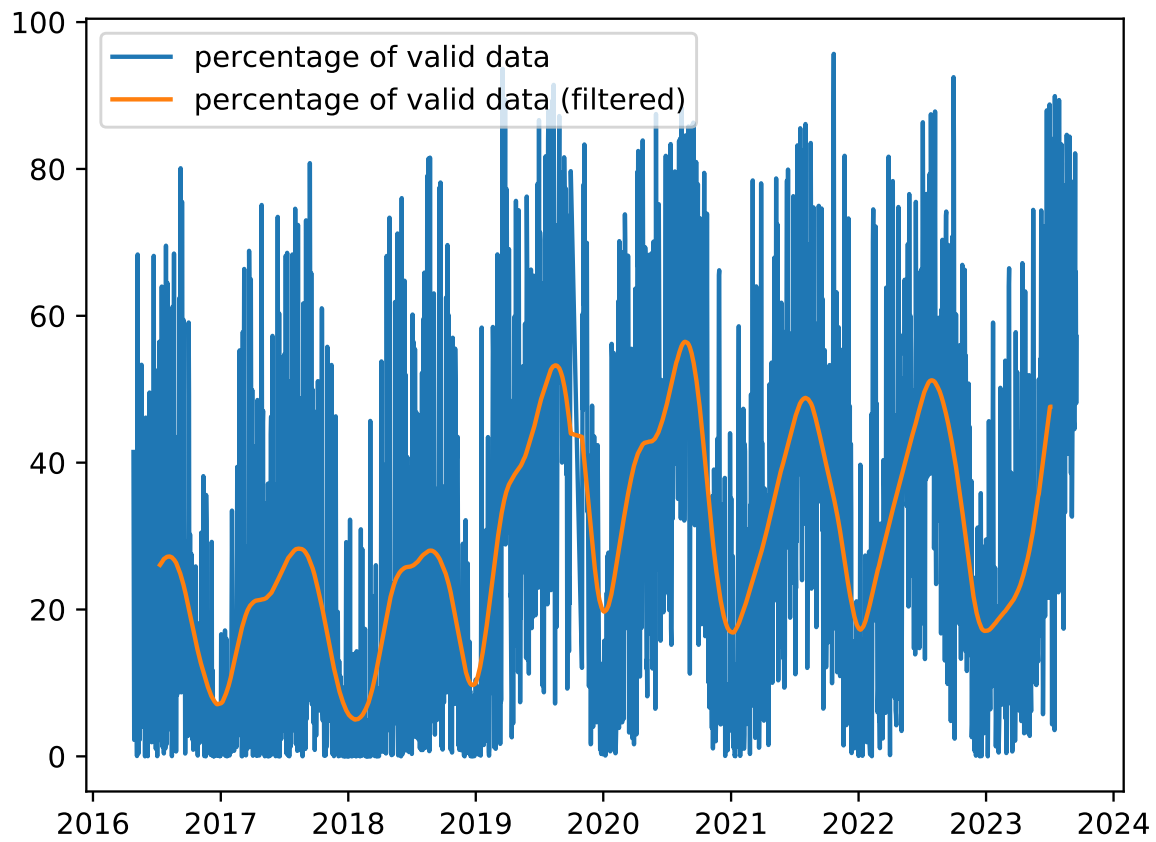
6

Figure 1. Percentage of valid data over time in each satellite image for the Black Sea dataset and percentage of valid data filtered by a Gaussian filter (with a standard deviation of 30 days).
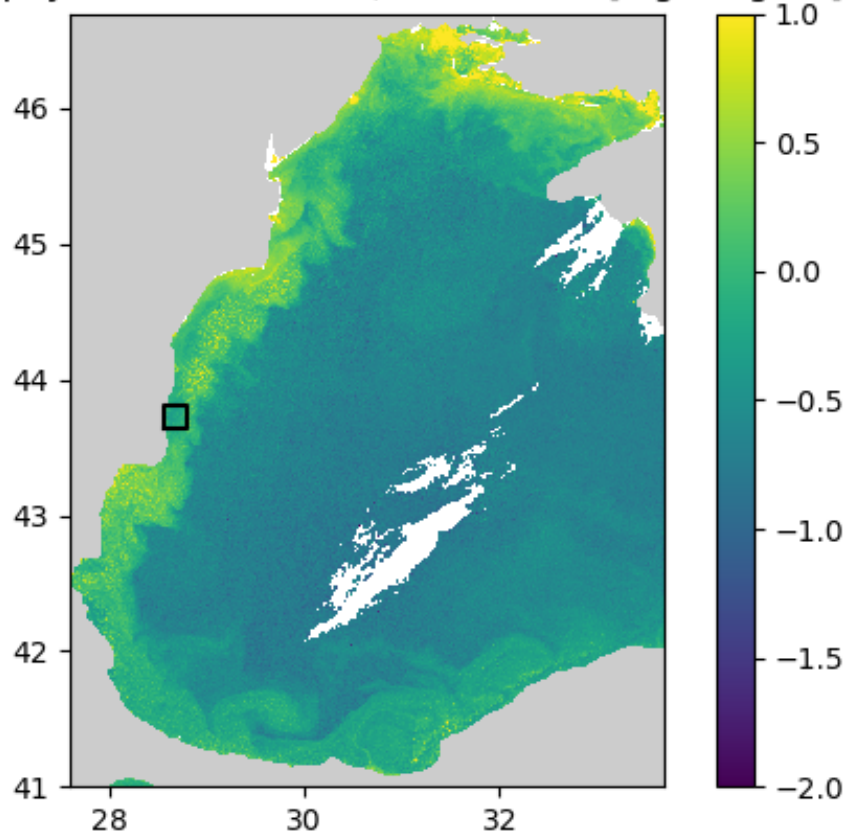
Figure 2. Western part of the Black Sea. The black square corresponds to the area where the methods are validated and tested (units: $\log_{10} \mathrm{mg\,m^{-3}}$).

4 Method

4.1 Training with clouded images

The training approach by Ho et al. (2020) assumes that we have a large training dataset with clear images. Unfortunately, for satellite observations, the clouds are so common that it would be difficult to create such a dataset. If the data was previously interpolated, then there is the risk that the neural network would also learn potential interpolation artifacts. Alternatively, the neural network could also be trained with data from a numerical model. But even in this case, the neural network would also learn biases and errors present in the model. When validating models with satellite observations, it is generally preferable that

the satellite observation is independent of a numerical model. Therefore, we are aiming to extend the approach of Ho et al. (2020) to train using images including clouds.

165 It is important to note that all operations in the training and sampling algorithms (equations 10 and 11) are only pointwise operations that do not involve the neighboring grid cells, except for the neural network which ensures spatial coherence. Rather than working with a global step t valid for a whole image, we consider the case where every pixel can be in a different state of degradation. The noise schedule β_t is a freely selectable list of parameters. For the following approach, we impose that $\beta_0 = 0$, which means that the noise is effectively added only at step 1 and later but not at step zero.

170 For a training image that contains clouds, we consider clouded pixels initially at the fully degraded level $t = T$ (i.e., normally distributed random noise) and clear pixels at the non-degraded level $t = 0$ (i.e., pixels as measured by the satellite). During training, for each image of the training dataset, a different image is randomly selected (also from the training dataset) and its cloud mask is used to degrade clear pixels of the input image (Figure 3). The stage of degradation t of these pixels is randomly chosen between 1 and T.

175

The loss function is the L2 norm between the actual added noise and the noise predicted by the neural network, computed over the pixels to which clouds have been added (Figure 4). Pixels who are clouded or covered by land are considered in the last stage of degradation (T) during training. Those pixels (in white on panel "added noise (target)" in Figure 4) cannot be used to evaluate the loss function, as the underlying value is not known (for clouded pixels) or not defined (for land pixels).
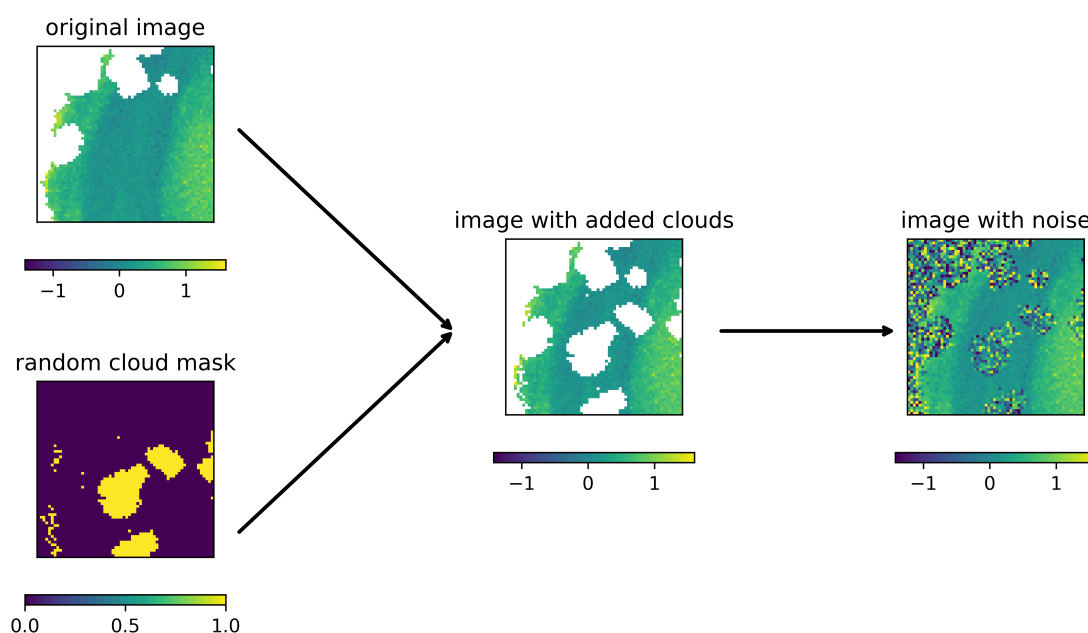

Figure 3. Data preparation for training. For the cloud mask, 1 corresponds to a clouded pixel and 0 to a pixel with valid data.
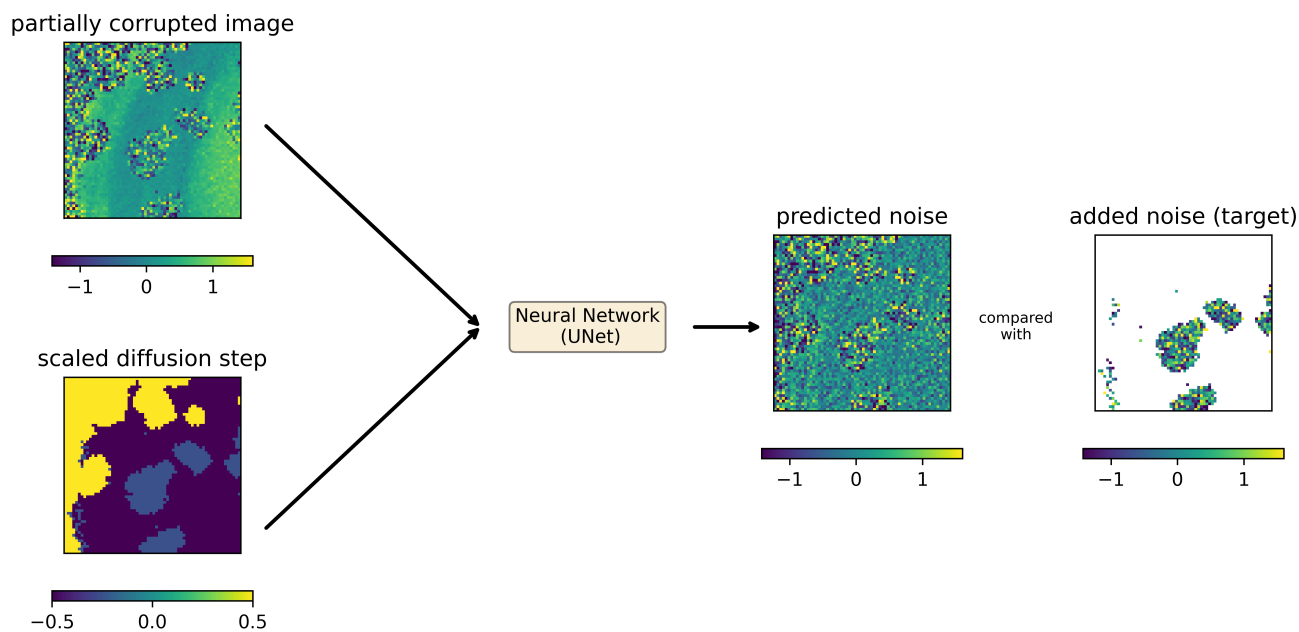
Figure 4. Input and output of the neural network during training. Predicted noise is an actual prediction of the trained diffusion model for the provided inputs (units: $\log_{10} \text{mg m}^{-3}$).
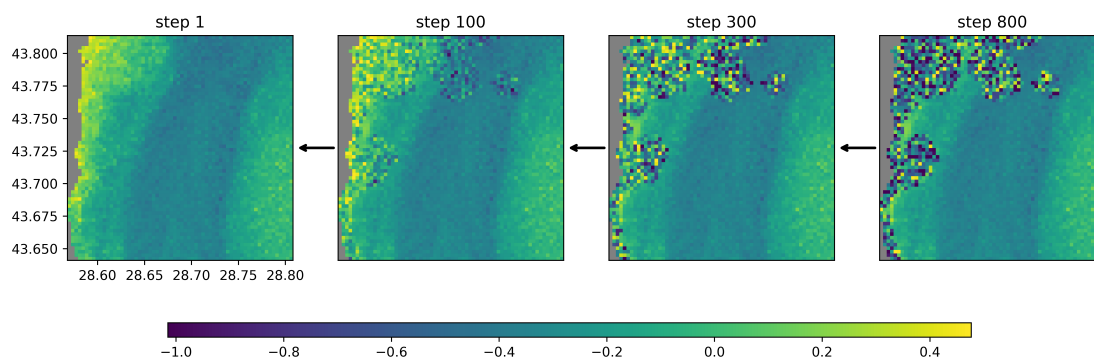

Figure 5. Reverse diffusion process illustrated with data from September 9, 2022 (units: $\log_{10} \text{mg m}^{-3}$).

180   The noise schedule of the forward diffusion process is defined by the parameter β_t, which varies linearly from 0 for $t = 0$ to a maximum value of β_{max} for $t = T$, where β_{max} and T are hyperparameters (chosen from a search range to satisfy $\bar{alpha}_T \approx 0$).

The neural network has the general architecture of a U-Net (Ronneberger et al., 2015) which is defined recursively by a block (at a given level l) composed of:

185   – three convolutional layers with output layers C_l and kernel size k_s followed each by an activation function.

   – 2-by-2 max pooling layer.

   – inner block at level $l-1$.

   – a single transpose convolution with a stride 2 with the number of output channels the same as the number of input channels of this block followed by an activation function.

190   – output of the previous layer, added to the input layer to form a residual connection.

An inner block at level $l-1$ has the same structure as an outer block at level l, except for level $l=1$, where the inner block is simply the identity function. This recursive definition of the U-Net architecture allows us to easily test networks with different depth levels. The depth level L, the number of channels C_l $(l=1\ldots L)$ and the kernel size k_s are hyperparameters of the network.

195   The input of the neural network is a 2D image with two channels. The first channel is the noisy image (normalized using the mean and standard deviation computed over the training dataset) and a 2D field with the step of the denoising pipeline (scaled between $-\frac{1}{2}$ and $\frac{1}{2}$). In this implementation of the denoising diffusion model, every pixel can be at a different step of degradation. The output of the neural network is a 2D field aiming to predict the noise that has been added to the input.

200   The model is optimized using the Adam optimizer (Kingma and Ba, 2014) using the default parameters except for the learning rate. During the training process, the learning rate is repeatedly reduced by a given factor after a certain number of steps. The initial learning rate, the number of steps between the reduction of the learning rate and the reduction factor are treated as a hyperparameter.

205   As usual, all model parameters (weights and biases of all convolutional layers) are optimized using the training data. The denoising diffusion model is implemented in the Julia programming language (Bezanson et al., 2017) using the deep learning library Flux.jl (Innes, 2018; Innes et al., 2018) and the GPU programming library CUDA.jl (Besard et al., 2019, 2018). The training of the neural network takes 7 hours on an NVIDIA A100-SXM4-40GB and 8 hours on an NVIDIA GeForce RTX 4090. All hyperparameters are determined using random search (Bergstra and Bengio, 2012) to minimize the RMS error of the
210   reconstruction with the validation data (Table 1). The optimal model (in terms of RMS error relative to the validation data) has in total 1.6 million parameters. Unless otherwise stated, all comparisons and reported validation metrics are performed with the independent test data, including the final validation. The final validation is performed using the independent test data.

Table 1. Hyperparameters of the diffusion model with the adopted value and the corresponding search space.

Parameter	Value	Search space
kernel size (k_s)	5	3 or 5
channels (C_l)	[16, 32, 64, 128]	[16, 32, 64, 128], [16, 32, 64, 128, 256] or [16, 32, 64, 128, 256, 256]
activation function	selu	relu, selu or swish
number of steps (T)	800	between 500 and 1500 (step of 100)
$\beta_{\max}$	0.027	between 0.01 and 0.04
batch size	60	fixed
number of epochs	100	fixed
learning rate	0.00017	between 10^{-5} and 0.0008
number of epochs before reducing the learning rate	50	between 10 and 100 (step of 10)
factor by which the learning rate is reduced	0.938	between 0.7 and 0.95

Preliminary experiments showed that a large training dataset is quite important to obtain a stable reconstruction. In fact, during the reverse diffusion, the neural network is applied 800 times to a satellite image to denoise it and to reconstruct the missing part of the image. Overfitting of the neural network, which emphasizes an unrealistic structure, could quickly lead to an unstable reverse diffusion process (i.e., the variance of the reconstructed image grows in an unbounded way). Such problems were resolved if a sufficiently large and diverse dataset was used for training. In particular, we needed to train the diffusion model using image tiles from the whole Black Sea to obtain a stable reverse diffusion process. As an illusion, a sample of the unconditional generation of images is shown in appendix A together with a random sample of the training data.

4.2 Sampling

After training the neural network, the missing data in the validation and test dataset are reconstructed. Every pixel clear of the input image is considered to be in the non-degraded state $t = 0$ and all other pixels (clouded or on land) in the fully degraded state $t = T$ initially. For the later pixels, the reverse diffusion process is used progressively to reduce their noise. The convolution operations in the U-Net ensure spatial coherence between clear pixels and reconstructed pixels. All clear pixels remain constant during the reverse diffusion because the corresponding term in equation (11) is zero as $\sigma_0 = \sqrt{\beta_0} = 0$ and

$\alpha_0 = 1 - \beta_0 = 1$ for these pixels.

For each image of the validation and test two datasets, the reconstruction process is repeated 64 times, leading to an ensemble of possible reconstructed fields. The larger the ensemble is, the more accurate the derived ensemble mean and variance. Various ensemble sizes have been used in the literature, for example the ECMWF real-time S2S forecasts use a 51 member ensemble size (Buizza et al., 2008). From this ensemble, the ensemble mean and the ensemble standard deviation are also computed. When minimizing the RMSE error relative to the validation dataset, only this ensemble mean is considered.

5 Results

Figures 6 and 7 show an example of the reconstruction for the dates August 7, 2022 and September 9, 2022 respectively from the test dataset. In the original data (panel a), additional clouds have been added using the cloud mask from a different image (panel b) in order to evaluate the accuracy of the reconstruction. From the data with the added clouds, the reverse diffusion process was performed 64 times. Two of these 64 reconstructions are shown in panels e and f. The ensemble mean (panel c) and the standard deviation (d) are also computed. Per construction, the interpolated fields in the pixels for which we have valid values in the input data is identical to the initial input value. The standard deviation there is thus consequently equal to zero. As expected, the ensemble mean is blurrier at the locations where we have added clouds, but the individual ensemble members also contain realistic small-scale information at these locations. In Figure 6 (panel d), we see that the ensemble standard deviation increases near fronts under clouds, since the exact position of the fronts cannot be deduced from the provided data. In general, the difference between the reconstructions is highest near the coastline, as the coastal areas are more variable than the offshore waters. This difference is particularly visible when large clouds are present near the coastline (Figure 7, panels d, e, and f).
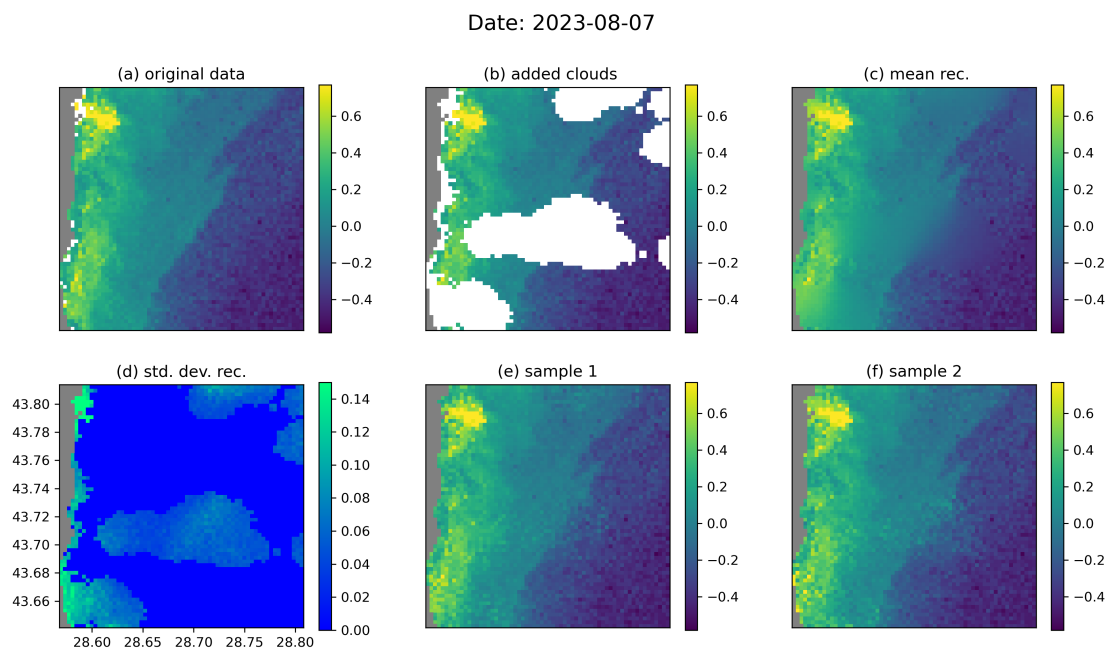
Figure 6. The denoising diffusion model applied on the independent test data for the date 2022-08-07 showing the original data (panel a), the data with added clouds (panel b), the ensemble mean and standard deviation (panel c, d) and two ensemble members (panel e and f). The units are $\log_{10} \mathrm{mg\,m^{-3}}$.
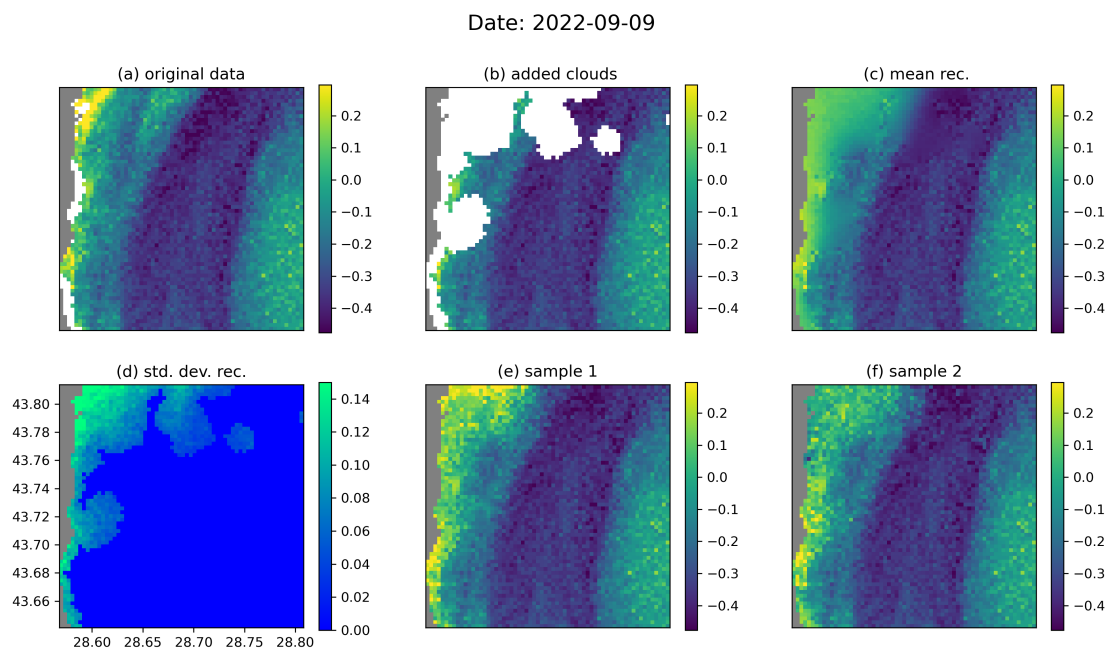
Date: 2022-09-09

Figure 7. The same as Figure 6 for the date September 9, 2022.

We compared the reconstruction with the DINCAE neural network. So far, DINCAE was only trained on data using a fixed area. We adopted the same approach here and trained DINCAE over the area used for validation. We used the same temporal split as the diffusion model: data before 2021-09-01 was used for training, the following 12-month period was used to adjust the hyperparameters (development dataset) and the last 12 months (starting on September 1, 2022) for the independent validation (test dataset). The hyperparameters adjusted using the development dataset were the number of epochs, the number of instances in the time window, the upsampling method and whether a refinement step is used. In Barth et al. (2020), it has been shown that the accuracy of a reconstruction can be improved by averaging the obtained reconstruction over a certain number of epochs after the epoch 200. The frequency (in number of epochs) of applying the neural network to the test and validation data to compute the corresponding average, is also a hyperparameter here. As before, the hyperparameters were determined by minimizing the RMS error relative to the validation dataset using random search. Table 2 shows all parameters used in DINCAE and their corresponding search range. The RMS error and the bias of DINCAE and the diffusion model are computed on artificially clouded pixels for the development and test dataset (3 and 4). In all cases, the bias is relatively low and does not contribute significantly to the RMS error. The RMS error of the diffusion model is slightly smaller than the RMS error of DINCAE for development and test dataset.

Table 2. Hyperparameters of DINCAE with the adopted value and the corresponding search space.

Parameter	Value	Search space
number of epochs	1276	between 500 and 1500
save epochs	36	between 10 and 40
batch size	32	fixed
channels	[32, 64, 128, 256, 512]	fixed
instances in time window	1	1, 3 or 5
upsampling method	nearest	nearest or bilinear
refinement step	desactivated	activated or deactivated

Table 3. Comparison of DINCAE and the diffusion model (using the ensemble mean) with the **development** dataset.

method	RMS	bias	std(reconstruction)	std(observation)
DINCAE	0.163	-0.0531	0.308	0.363
Diffusion Model	0.151	0.00568	0.333	0.363

Table 4. Comparison of DINCAE and the diffusion model (using the ensemble mean) with the **test** dataset.

method	RMS	bias	std(reconstruction)	std(observation)
DINCAE	0.175	0.0488	0.308	0.331
Diffusion Model	0.163	0.00388	0.285	0.331

Figure 8 shows a meandering coastal front with submesoscale flow features, which is partially obscured by the added clouds. The general structure of the front is preserved well by DINCAE and the diffusion model (panels c and e) but the level of details and the intensity is better represented using the diffusion model. The noise visible offshore is retained by the diffusion model (per construction), but it is effectively reduced by DINCAE which can be a desirable effect for some applications.
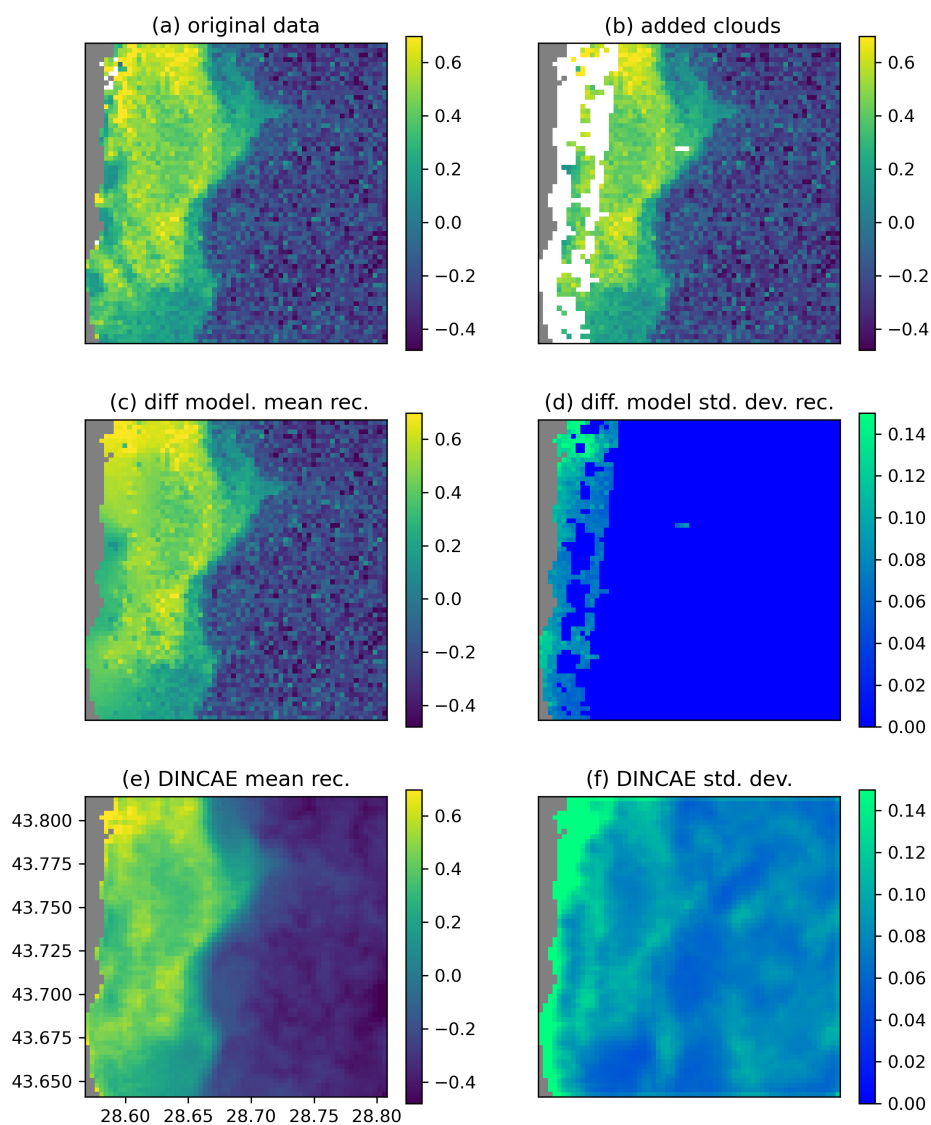
Date: 2022-11-10

Figure 8. Comparison between DINCAE and the diffusion model for the date November 10, 2022 (units: $\log_{10} \, \mathrm{mg} \, \mathrm{m}^{-3}$).

265 To assess the scales present in the reconstructed data, a variogram (Cressie, 1991; Wackernagel, 2003) is computed using the reconstruction of the development and test datasets (Figure 9). A variogram of a spatial random field $\phi(\mathbf{x})$ is defined by the following expectation:

$$2\gamma(\mathbf{x}_1, \mathbf{x}_2) = E\left[(\phi(\mathbf{x}_1) - \phi(\mathbf{x}_2))^2\right] \tag{12}$$

Here we are considering a variogram only as a function of a distance $h = \|\mathbf{x}_1 - \mathbf{x}_2\|^2$ which allows us to estimate the vari-
270 ogram numerically by computing the squared difference for the field at randomly chosen locations. These squared differences are averaged over bins of their distances using all time instances of the validation and test datasets. For the diffusion model, the variogram is deduced using the individual ensemble members. When computing the variogram of the original data, only the pairs of points corresponding both to valid pixels are considered.

275 It can be seen from Figure 9 that both reconstruction methods underestimate the variance in the original data to some degree, but the reconstruction with the diffusion model is consistently closer to the original data than DINCAE, which confirms our qualitative assessment of Figure 8. For the independent test dataset and scales larger than 15 km, the variogram of the diffusion model coincides with the variogram of the original data. The fact that the variogram does not converge to zero as distances tend to zero shows that the data is affected by spatially white noise, as it can be seen in the offshore region of Figure 8 (panel
280 a) which is also called the "nugget effect" (Matheron, 1962).
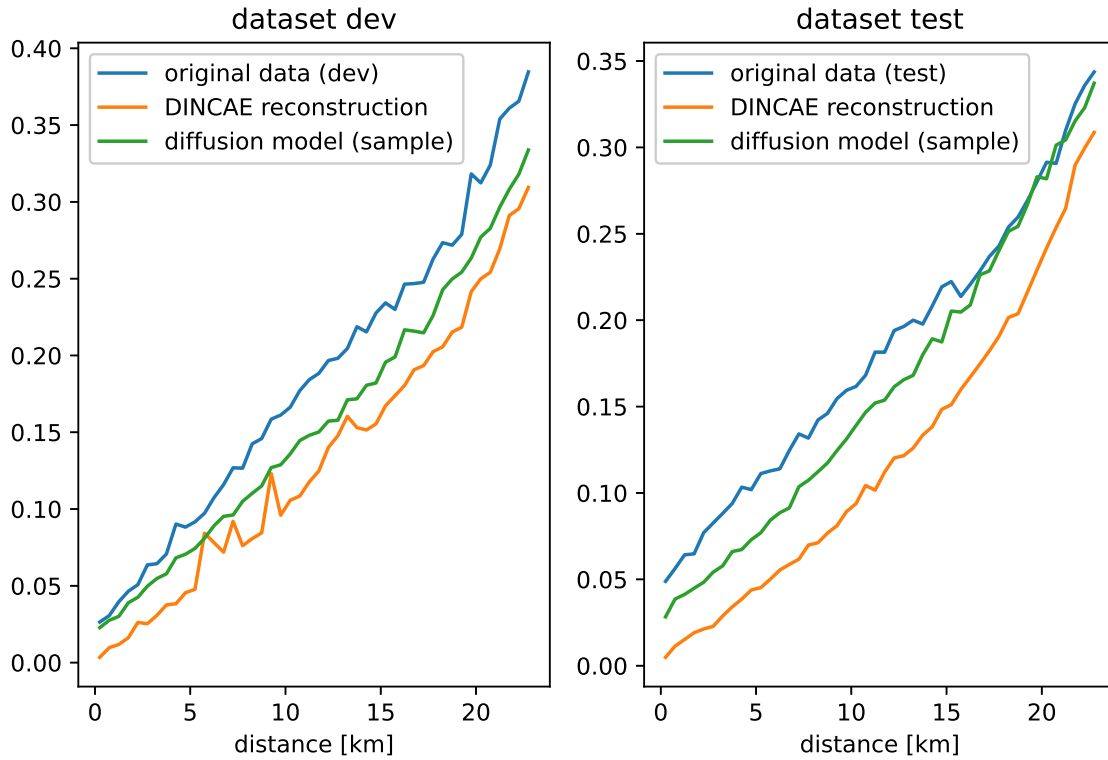
18

Figure 9. Variogram of the development (dev) and test datasets (units: $(\log_{10} \text{mg m}^{-3})^2$).

To assess the statistical reliability of the produced reconstruction ensemble, we can use the so-called Talagrand diagram, also called rank histogram (Talagrand et al., 1997; Hamill, 2001). If the ensemble is generated from the same probability distribution as the observations, the ensemble is considered reliable. For each pixel for which an observation is available, the corresponding value of all 64 ensemble members is sorted by $x_1 \leq x_2 \cdots \leq x_N$ (where here $N = 64$), and the following successive $N + 1$ bins are defined as:

$$b_0 \quad = \quad (-\infty, x_1) \tag{13}$$
$$b_i \quad = \quad [x_i, x_{i+1}) \quad \text{for} \quad i = 1 \ldots N - 1 \tag{14}$$
$$b_N \quad = \quad [x_N, \infty) \tag{15}$$

In this case, the probability that the observations belong to the interval b_i is $\frac{1}{N+1}$ and thus independent of the value of the observation. With a sufficient number of observations, this probability can be estimated for different bins i. A Talagrand diagram shows these frequencies as a function of the bin indices. A perfectly reliable ensemble would result in a flat curve.

Underdispersive (or overdispersive) ensembles would result in a ∪-shaped (respectively ∩-shaped) curve.

Figure 10 shows the Talagrand diagram computed for the development and testing dataset. It can be seen that except for the
295   two first and two last bins (corresponding to the probabilities between 3% and 97%), the Talagrand diagram is relatively flat.
This shows that the produced probabilities are reliable, except for very rare events where the produced ensemble is underdispersive. The difficulty of predicting rare events is a known issue in machine learning (*e.g.* Kaiser et al., 2017) and a dedicated area of research.
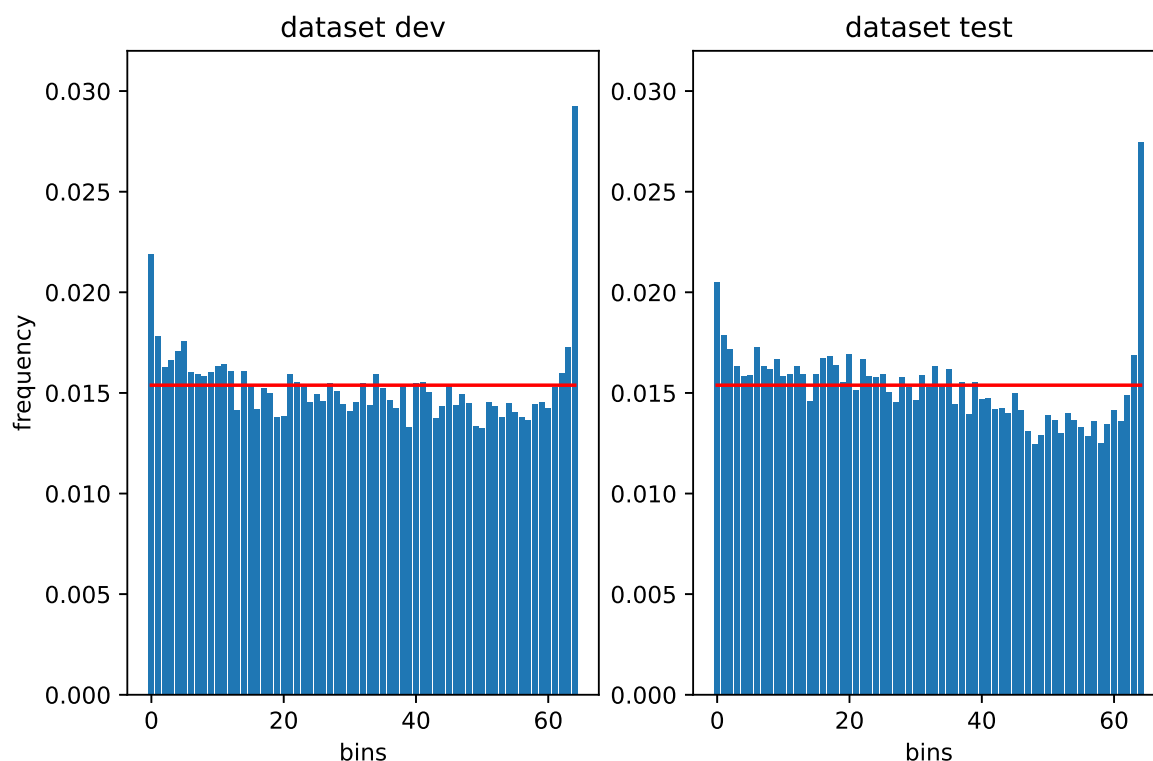
Figure 10. Talagrand diagram of the development (dev) and test datasets.

Another common probabilistic validation approach is the Continuous-Ranked Probability Score (CRPS). Following Hers-
300   bach (2000), it is defined as:

$$\text{CRPS} = \int_{-\infty}^{\infty} (P(x) - H(x - x_o))^2 dx \tag{16}$$

where $P(x)$ is the cumulative distribution function, x_o the observations, and $H(x)$ the Heaviside function ($H(x) = 1$ for $x \geq 0$ and $H(x) = 0$ otherwise). The CRPS has the same units as the data x and it is always positive or zero. When applied to ensemble reconstructions, the CRPS attains its best score of zero, only when all ensemble members reproduce the observations exactly. The CRPS can be decomposed into potential CRPS ($\mathrm{CRPS_{pot}}$), reliability, uncertainty and resolution:

$$\mathrm{CRPS} = \mathrm{reliability} + \mathrm{CRPS_{pot}} \tag{17}$$

$$\mathrm{CRPS_{pot}} = \mathrm{uncertainty} - \mathrm{resolution} \tag{18}$$

The reliability (smaller is better) measures whether the ensemble accurately reflects the uncertainty of the results. Note that a system reproducing the climatological data distribution would be perfectly reliable but would not resolve different events. The resolution (higher is better) determines whether the ensemble allows discrimination between different events. The resolution would be zero for the data climatology. Consequently, the uncertainty is the CRPS score for the data climatology and thus depends only on the variability of the data (and not on the reconstruction method). For more information on these scores and how they are computed based on an ensemble, the reader is referred to Hersbach (2000) and Candille et al. (2007). It should be noted that in this context, the resolution is not related to the spatial or temporal resolution of the dataset.

Table 5 shows the corresponding scores for the test and development datasets. All scores have the same units of the data and the standard deviation of this training data is $0.46 \log_{10} \mathrm{mg\,m^{-3}}$ to provide an order of magnitude of the variability. The reliability of the diffusion model seems to be quite good, which confirms the results of the Talagrand diagram (Figure 10). The CRPS is mostly determined by the resolution. To further improve the resolution, it might be beneficial to use more data (including multivariate reconstructions), but it is clear that a perfect score is not attainable simply due to the lack of information under clouds.

Table 5. Decomposition of the CRPS score (units $\log_{10} \mathrm{mg\,m^{-3}}$).

dataset	CRPS	reliability	CRPS$_{\mathrm{pot}}$	resolution	uncertainty
dev	0.0635	0.00045	0.0631	0.13	0.193
test	0.0712	0.000405	0.0708	0.112	0.182

6   Conclusions

Denoising diffusion models have shown their great potential for image generation for computer vision applications and related tasks. One limitation of this approach, in the context of satellite data, is that it requires clear images for training. The present manuscript shows that the training approach of Ho et al. (2020) can be extended if the training dataset contains incomplete images. The approach presented here does not need any additional parameters that would require calibration. The spatial coherence and the statistical reliability of the resulting reconstruction process emerges naturally from the training.

The method is tested on relatively small images of the chlorophyll a concentration of the Black Sea. The quality of the reconstruction is assessed using independent test data. The diffusion method compared favorably against the U-Net DINCAE.

330 The RMS error of the reconstructed data using the denoising diffusion model was smaller than the corresponding reconstruction of DINCAE. The main advantage of the diffusion model is however the ability to reproduce an ensemble of possible reconstructed conditions on the available data. Each of these reconstructions contains small-scale information comparable to the scales of variability in the original data, avoiding a common problem where the results of U-Net and autoencoders produce images that are too smooth, as the information on small scales can typically not be recovered under clouds with a certain extent.

335

The ensembles of reconstructed data generated by the diffusion model can be used, for example, in the detection of gradients and fronts in the satellite images or in the estimation of the error in derived quantities, where information on how the error is correlated in space is also needed.

340 Another aspect that would be important to investigate in future studies would be the ability to reconstruct sequences of images, multivariate reconstructions and data with inhomogeneous and/or very reduced coverage like *in situ* observations. It remains to be seen how well the diffusion model can be used in these cases.

345 *Author contributions.* AB designed and implemented the neural network. AB, JB, AAA, BM, CT and JMB contributed to the discussions and to the writing of the manuscript.

Competing interests. Aida Alvera Azcárate is a member of the editorial board of the journal Ocean Science.

References

Alvera-Azcárate, A., Barth, A., Parard, G., and Beckers, J.-M.: Analysis of SMOS sea surface salinity data using DINEOF, Remote Sensing of Environment, 180, 137 – 145, https://doi.org/10.1016/j.rse.2016.02.044, special Issue: ESA's Soil Moisture and Ocean Salinity Mission - Achievements and Applications, 2016.

Alvera-Azcàrate, A., Van der Zande, D., Barth, A., Troupin, C., Martin, S., and Beckers, J.-M.: Analysis of 23 years of daily cloud-free chlorophyll and suspended particulate matter in the Greater North Sea, Frontiers in Marine Science, 8, https://doi.org/10.3389/fmars.2021.707632, 2021.

Barth, A., Alvera-Azcárate, A., Licer, M., and Beckers, J.-M.: DINCAE 1.0: a convolutional neural network with error estimates to reconstruct sea surface temperature satellite observations, Geoscientific Model Development, 13, 1609–1622, https://doi.org/10.5194/gmd-13-1609-2020, 2020.

Barth, A., Alvera-Azcárate, A., Troupin, C., and Beckers, J.-M.: DINCAE 2.0: multivariate convolutional neural network with error estimates to reconstruct sea surface temperature satellite and altimetry observations, Geoscientific Model Development, https://doi.org/10.5194/gmd-2021-353, 2022.

Bayat, R.: A Study on Sample Diversity in Generative Models: GANs vs. Diffusion Models, https://openreview.net/forum?id=BQpCuJoMykZ, 2023.

Bergstra, J. and Bengio, Y.: Random Search for Hyper-Parameter Optimization, Journal of Machine Learning Research, 13, 281–305, http://www.jmlr.org/papers/v13/bergstra12a.html, 2012.

Besard, T., Foket, C., and De Sutter, B.: Effective Extensible Programming: Unleashing Julia on GPUs, IEEE Transactions on Parallel and Distributed Systems, https://doi.org/10.1109/TPDS.2018.2872064, 2018.

Besard, T., Churavy, V., Edelman, A., and De Sutter, B.: Rapid software prototyping for heterogeneous and distributed platforms, Advances in Engineering Software, 132, 29–46, 2019.

Bezanson, J., Edelman, A., Karpinski, S., and Shah, V. B.: Julia: A fresh approach to numerical computing, SIAM review, 59, 65–98, https://doi.org/10.1137/141000671, 2017.

Buizza, R., Leutbecher, M., and Isaksen, L.: Potential use of an ensemble of analyses in the ECMWF Ensemble Prediction System, Quarterly Journal of the Royal Meteorological Society, 134, 2051–2066, https://doi.org/https://doi.org/10.1002/qj.346, 2008.

Candille, G., Côté, C., Houtekamer, P. L., and Pellerin, G.: Verification of an Ensemble Prediction System against Observations, Monthly Weather Review, 135, 2688–2699, https://doi.org/10.1175/MWR3414.1, 2007.

Cressie, N.: Statistics for Spatial Data, A Wiley-interscience publication, J. Wiley, ISBN 9780471843368, 1991.

Dhariwal, P. and Nichol, A.: Diffusion Models Beat GANs on Image Synthesis, in: Advances in Neural Information Processing Systems, edited by Ranzato, M., Beygelzimer, A., Dauphin, Y., Liang, P., and Vaughan, J. W., vol. 34, pp. 8780–8794, Curran Associates, Inc., https://proceedings.neurips.cc/paper_files/paper/2021/file/49ad23d1ec9fa4bd8d77d02681df5cfa-Paper.pdf, 2021.

European Union-Copernicus Marine Service: Black Sea, Bio-Geo-Chemical, L3, daily Satellite Observations (1997-ongoing), https://doi.org/10.48670/moi-00303, dataset accessed 2023-09-26, dataset ID `cmems_obs-oc_blk_bgc-plankton_my_l3-olci-300m_P1D`, 2022.

Evensen, G.: Data assimilation: the Ensemble Kalman Filter, 2nd edition, Springer, https://doi.org/10.1007/978-3-642-03711-5, 2009.

Feller, W.: On the Theory of Stochastic Processes, with Particular Reference to Applications, in: Berkeley Symp. on Math. Statist. and Prob., pp. 403–432, 1949.

Feng, L. and Hu, C.: Comparison of Valid Ocean Observations Between MODIS Terra and Aqua Over the Global Oceans, IEEE Transactions on Geoscience and Remote Sensing, 54, 1575–1585, https://doi.org/10.1109/tgrs.2015.2483500, 2016.

Goh, E., Yepremyan, A. R., Wang, J., and Wilson, B.: MAESSTRO: Masked Autoencoders for Sea Surface Temperature Reconstruction under Occlusion, EGUsphere, 2023, 1–20, https://doi.org/10.5194/egusphere-2023-1385, 2023.

Goodfellow, I., Bengio, Y., and Courville, A.: Deep Learning, MIT Press, http://www.deeplearningbook.org, 2016.

Hamill, T. M.: Interpretation of Rank Histograms for Verifying Ensemble Forecasts, Monthly Weather Review, 129, 550–560, https://doi.org/10.1175/1520-0493(2001)129<0550:IORHFV>2.0.CO;2, 2001.

Han, Z., He, Y., Liu, G., and Perrie, W.: Application of DINCAE to Reconstruct the Gaps in Chlorophyll-a Satellite Observations in the South China Sea and West Philippine Sea, Remote Sensing, 12, https://doi.org/10.3390/rs12030480, 2020.

Hersbach, H.: Decomposition of the Continuous Ranked Probability Score for Ensemble Prediction Systems, Weather and Forecasting, 15, 559–570, https://doi.org/10.1175/1520-0434(2000)015<0559:DOTCRP>2.0.CO;2, 2000.

Ho, J. and Salimans, T.: Classifier-Free Diffusion Guidance, https://doi.org/10.48550/arXiv.2207.12598, 2022.

Ho, J., Jain, A., and Abbeel, P.: Denoising Diffusion Probabilistic Models, in: NIPS'20: Proceedings of the 34th International Conference on Neural Information Processing Systems, 574, pp. 6840–6851, 2020, https://doi.org/10.48550/arXiv.2006.11239, 2020.

Hong, Z., Long, D., Li, X., Wang, Y., Zhang, J., Hamouda, M. A., and Mohamed, M. M.: A global daily gap-filled chlorophyll-a dataset in open oceans during 2001–2021 from multisource information using convolutional neural networks, Earth System Science Data, 15, 5281–5300, https://doi.org/10.5194/essd-15-5281-2023, 2023.

Innes, M.: Flux: Elegant Machine Learning with Julia, Journal of Open Source Software, https://doi.org/10.21105/joss.00602, 2018.

Innes, M., Saba, E., Fischer, K., Gandhi, D., Rudilosso, M. C., Joy, N. M., Karmali, T., Pal, A., and Shah, V.: Fashionable Modelling with Flux, CoRR, abs/1811.01457, https://arxiv.org/abs/1811.01457, 2018.

Jensen, J. L. W. V.: Sur les fonctions convexes et les inégalités entre les valeurs moyennes, Acta Mathematica, 30, 175–193, https://doi.org/10.1007/bf02418571, 1906.

Ji, C., Zhang, Y., Cheng, Q., and Tsou, J. Y.: Investigating ocean surface responses to typhoons using reconstructed satellite data, International Journal of Applied Earth Observation and Geoinformation, 103, 102 474, https://doi.org/10.1016/j.jag.2021.102474, 2021.

Jung, S., Yoo, C., and Im, J.: High-Resolution Seamless Daily Sea Surface Temperature Based on Satellite Data Fusion and Machine Learning over Kuroshio Extension, Remote Sensing, 14, 575, https://doi.org/10.3390/rs14030575, 2022.

Kaiser, L., Nachum, O., Roy, A., and Bengio, S.: Learning to Remember Rare Events, CoRR, abs/1703.03129, http://arxiv.org/abs/1703.03129, 2017.

Kajiyama, T., D'Alimonte, D., and Zibordi, G.: Algorithms Merging for the Determination of Chlorophyll-a Concentration in the Black Sea, IEEE Geoscience and Remote Sensing Letters, 16, 677–681, https://doi.org/10.1109/lgrs.2018.2883539, 2019.

Kingma, D. P. and Ba, J.: Adam: A Method for Stochastic Optimization, CoRR, abs/1412.6980, http://arxiv.org/abs/1412.6980, 2014.

Lee, Z., Carder, K. L., and Arnone, R. A.: Deriving inherent optical properties from water color: a multiband quasi-analytical algorithm for optically deep waters, Applied Optics, 41, 5755, https://doi.org/10.1364/ao.41.005755, 2002.

Lugmayr, A., Danelljan, M., Romero, A., Yu, F., Timofte, R., and Gool, L. V.: RePaint: Inpainting using Denoising Diffusion Probabilistic Models, 2022.

Luo, X., Song, J., Guo, J., Fu, Y., Wang, L., and Cai, Y.: Reconstruction of chlorophyll-a satellite data in Bohai and Yellow sea based on DINCAE method, International Journal of Remote Sensing, 43, 3336–3358, https://doi.org/10.1080/01431161.2022.2090872, 2022.

Matheron, G.: Traité de géostatistique appliquée, no. v. 1 in Memoires, Éditions Technip, 1962.

430 Mikelsons, K. and Wang, M.: Optimal satellite orbit configuration for global ocean color product coverage, Opt. Express, 27, A445–A457, https://doi.org/10.1364/OE.27.00A445, 2019.

Pujol, C., Pérez-Santos, I., Barth, A., and Alvera-Azcàrate, A.: Marine Heatwaves Offshore Central and South Chile: Understanding Forcing Mechanisms During the Years 2016-2017, Frontiers in Marine Science, 9, https://doi.org/10.3389/fmars.2022.800325, 2022.

Reynolds, R. W., Smith, T. M., Liu, C., Chelton, D. B., Casey, K. S., and Schlax, M. G.: Daily High-resolution Blended Analyses for sea
435 surface temperature, Journal of Climate, 20, 5473–5496, https://doi.org/10.1175/2007JCLI1824.1, 2007.

Ronneberger, O., Fischer, P., and Brox, T.: U-Net: Convolutional Networks for Biomedical Image Segmentation, in: Medical Image Computing and Computer-Assisted Intervention – MICCAI 2015, edited by Navab, N., Hornegger, J., Wells, W. M., and Frangi, A. F., pp. 234–241, Springer International Publishing, Cham, ISBN 978-3-319-24574-4, https://doi.org/10.1007/978-3-319-24574-4_28, 2015.

Saharia, C., Ho, J., Chan, W., Salimans, T., Fleet, D. J., and Norouzi, M.: Image Super-Resolution via Iterative Refinement,
440 https://doi.org/10.48550/ARXIV.2104.07636, 2021.

Saulquin, B., Gohin, F., and Garrello, R.: Regional Objective Analysis for Merging High-Resolution MERIS, MODIS/Aqua, and SeaWiFS Chlorophyll- a Data From 1998 to 2008 on the European Atlantic Shelf, IEEE Transactions on Geoscience and Remote Sensing, 49, 143–154, https://doi.org/10.1109/TGRS.2010.2052813, 2011.

Sohl-Dickstein, J., Weiss, E., Maheswaranathan, N., and Ganguli, S.: Deep Unsupervised Learning using Nonequilibrium Thermodynamics,
445 in: Proceedings of the 32nd International Conference on Machine Learning, edited by Bach, F. and Blei, D., vol. 37 of *Proceedings of Machine Learning Research*, pp. 2256–2265, PMLR, Lille, France, 2015.

Talagrand, O., Vautard, R., and Strauss, B.: Evaluation of probabilistic prediction systems, in: Proceedings, ECMWF Workshop on Predictability, pp. 1–25, ECMWF, 1997.

Wackernagel, H.: Multivariate Geostatistics: an introduction with applications, Springer-Verlag, 3rd edn., 2003.

450 Wylie, D., Jackson, D. L., Menzel, W. P., and Bates, J. J.: Trends in Global Cloud Cover in Two Decades of HIRS Observations, Journal of Climate, 18, 3021–3031, https://doi.org/10.1175/JCLI3461.1, 2005.

Yadav, C. and Bottou, L.: Cold Case: The Lost MNIST Digits, in: Advances in Neural Information Processing Systems, edited by Wallach, H., Larochelle, H., Beygelzimer, A., d'Alché-Buc, F., Fox, E., and Garnett, R., vol. 32, Curran Associates, Inc., https://proceedings.neurips.cc/paper_files/paper/2019/file/51c68dc084cb0b8467eafad1330bce66-Paper.pdf, 2019.

455 Zibordi, G., Mélin, F., Berthon, J.-F., and Talone, M.: In situ autonomous optical radiometry measurements for satellite ocean color validation in the Western Black Sea, Ocean Science, 11, 275–286, https://doi.org/10.5194/os-11-275-2015, 2015.

Appendix A: Sample of training data and generated images

In Figure A1, a random sample of training images are shown. Most training images are affected by a significant amount of noise and some artifacts are present in the training data. The denoising diffusion model aims to generate images with the same distribution and therefore including the noise and artifacts.
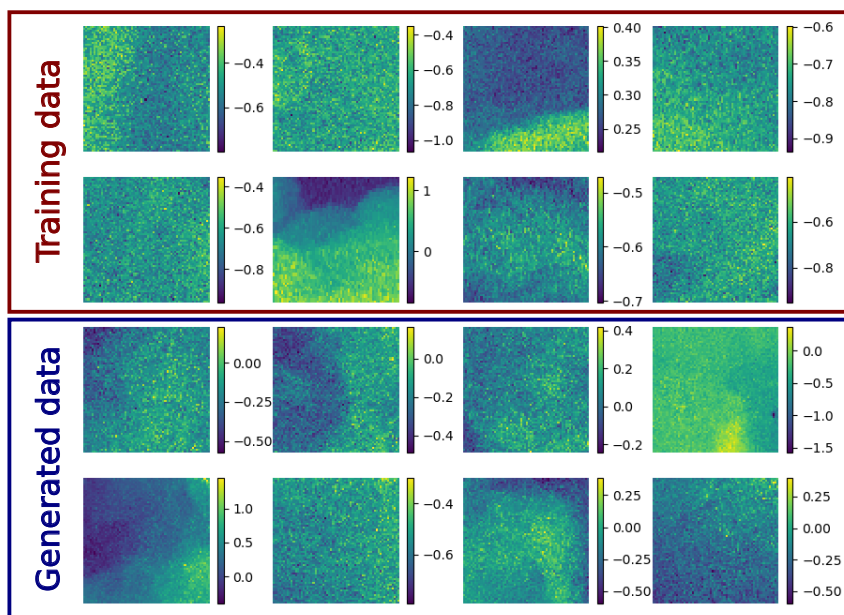

Figure A1. Sample of training data and generated images (starting an entirely masked input image)